


Electrochemical Activation-Induced Structural Transformation in Ni(OH)₂/Ti₃C₂T_x/NF Systems with Enhanced Electrochemical Performance for Hybrid Supercapacitors

Chuming Xu, Lu Dai, Yiming Zhao, Shuang Li*, Yapan Wu, Xueqian Wu, Gaixia Zhang, Shuhui Sun* , and Dongsheng Li*

Exploring a novel strategy for large-scale production of battery-type Ni(OH)₂-based composites, with excellent capacitive performance, is still greatly challenging. Herein, we developed a facile and cost-effective strategy to in situ grow a layer of Ni(OH)₂/Ti₃C₂T_x composite on the nickel foam (NF) collector, where Ti₃C₂T_x is not only a conductive component, but also a catalyst that accelerates the oxidation of NF to Ni(OH)₂. Detailed analysis reveals that the crystallinity, morphology, and electronic structure of the integrated electrode can be tuned via the electrochemical activation, which is beneficial for improving electrical conductivity and redox activity. As expected, the integrated electrode shows a specific capacity of 1.09 C cm⁻² at 1 mA cm⁻² after three custom activation cycles and maintains 92.4% of the initial capacity after 1500 cycles. Moreover, a hybrid supercapacitor composed of Ni(OH)₂/Ti₃C₂T_x/NF cathode and activated carbon anode provides an energy density of 0.1 mWh cm⁻² at a power density of 0.97 mW cm⁻², and excellent cycling stability with about 110% capacity retention rate after 5000 cycles. This work would afford an economical and convenient method to steer commercial Ni foam into advanced Ni(OH)₂-based composite materials as binder-free electrodes for hybrid supercapacitors.

1. Introduction

Hybrid supercapacitors (HSCs) composed of battery-type and capacitive-type electrodes demonstrate comprehensive merits from both battery and supercapacitor devices, which are expected to achieve high energy and power density.^[1-4] Efficient battery-type electrode materials are the key to fabricating high-performance HSCs.^[5-7] Among the battery-type electrode materials discovered so far, Ni(OH)₂ is considered to be one of the most promising materials owing to its high theoretical specific capacity, abundant resources, and environmental friendliness.^[8-11] However, in practical applications, Ni(OH)₂ often exhibits lower energy storage capacity and poor cycling stability due to the inherently weak electrical conductivity and serious volume expansion during the charging-discharging process.^[12-14] To solve these problems, an effective strategy is contacting Ni(OH)₂ with the current collector closely or adding other conductive materials to form composites.^[15-17] Under such circumstances, preparing binder-free Ni(OH)₂/NF integrated

electrode through the direct oxidation of nickel foam (NF) collector attracts our attention, which not only can effectively prevent the shedding of the Ni(OH)₂ to ensure long-term stability, but also is conducive to large-scale production and charge transfer.^[18,19] However, the areal specific capacity or stability of the single Ni(OH)₂/NF is still unsatisfactory. Adding conductive materials into the NF-oxidation system to in situ prepare Ni(OH)₂-based hybrids on NF collector can further increase electrical conductivity and durability, but this is rarely reported. Therefore, it is necessary to develop a facile and economical modified NF-oxidation route for designing high-performance Ni(OH)₂-based composite electrode materials.

Except for the design of materials, electrochemical activation is often used to boost the energy storage capacity of electrode materials.^[20] During the electrochemical process, some weak materials can be converted into highly active components, and/or the microstructure changes of materials can enhance electrochemical activity.^[21,22] For instance, graphene derivatives or oxygen-containing groups can be introduced in carbon-based materials, after the electrochemical cycle, to

C. Xu, L. Dai, Y. Zhao, Dr. S. Li, Dr. Y.-P. Wu, Dr. X. Wu, Prof. D. Li
College of Materials and Chemical Engineering, Key Laboratory of Inorganic
Nonmetallic Crystalline and Energy Conversion Materials, China Three
Gorges University, Yichang 443002, China

Hubei Three Gorges Laboratory, Yichang 443007, China

E-mail: lishmail@126.com

E-mail: lidongsheng1@126.com


Prof. G. Zhang

Department of Electrical Engineering, École de Technologie Supérieure (ÉTS),
Montréal, Québec H3C 1K3, Canada

Prof. S. Sun

Institut National de la Recherche Scientifique (INRS), Centre Énergie
Matériaux Télécommunications, Varennes, Québec J3X 1P7, Canada

E-mail: shuhui.sun@inrs.ca

 The ORCID identification number(s) for the author(s) of this article
can be found under <https://doi.org/10.1002/eam2.12672>.

DOI: 10.1002/eam2.12672

improve the specific capacitance value.^[23,24] Zhang et al. found that the as-sputtered MnO_2 films could be transformed into ultrathin nanosheets with different content of embedded Na^+ ions during the electrochemical activation process of $\text{MnO}_2\text{-NS@CNTs}$, resulting in enhanced surface and diffusion controlled capacitance processes.^[25] Such a phenomenon has also occurred for Ni(OH)_2 . For instance, Zou et al. reported that the energy storage capacity of Ni(OH)_2 increased after the cyclic voltammetry (CV) or galvanostatic charge/discharge (GCD) activation process, where the layered porous network Ni(OH)_2 nanostructure was prepared by GCD process, while the spherical stacking nanostructures were generated by CV process.^[26] However, the understanding and exploration of the electrochemical activation of Ni(OH)_2 -based materials are still very limited. Especially, the relationship between material structure and performance needs further in-depth research.

Recently, the popular MXene (metal carbide/nitride nanosheet) materials with metallic conductivity and abundant hydrophilic termination groups have provided inspiration as potential conductive substrates for the preparation of tightly coupled composites.^[27–31] Bearing these in mind, we started with constructing $\text{Ni(OH)}_2/\text{Ti}_3\text{C}_2\text{T}_x$ MXene composite on NF through mild $\text{Ti}_3\text{C}_2\text{T}_x$ and hydrogen peroxide (H_2O_2) oxidation route under a hydrothermal condition. Detailed experimental results showed that NF was partially oxidized by the H_2O_2 under the role of $\text{Ti}_3\text{C}_2\text{T}_x$, which resulted in the in situ generation of a layer of Ni(OH)_2 on the NF skeleton. In addition, $\text{Ti}_3\text{C}_2\text{T}_x$ was tightly coupled with Ni(OH)_2 to form $\text{Ni(OH)}_2/\text{Ti}_3\text{C}_2\text{T}_x/\text{NF}$ integrated electrode. More interestingly, electrochemical activation can not only tune the morphology and electronic structure of the integrated electrodes, but also transform the original weak crystallinity of Ni(OH)_2 into the good crystallinity. These changes are responsible for the dramatically increased specific capacity from 0.28 to 1.09 C cm^{-2} and the maintenance of capacity of 92.4% after 1500 cycles. Moreover, a

hybrid supercapacitor composed of $\text{Ni(OH)}_2/\text{Ti}_3\text{C}_2\text{T}_x/\text{NF}$ cathode and activated carbon anode could provide an energy density of 0.1 mWh cm^{-2} at a power density of 0.97 mW cm^{-2} , and excellent cycling stability with about 110% capacity retention rate after 5000 cycles, holding great promise for energy storage applications. This synthesis method developed here has significant advantages of facile, cost-effective, and additive-free processing, which is conducive to large-scale production and affords an interesting direction for preparing advanced self-supported composite electrode materials.

2. Results and Discussion

The preparation process of the integrated electrode is shown in **Figure 1**, which mainly involves the synthesis of $\text{Ti}_3\text{C}_2\text{T}_x$ nanosheets, and the subsequent oxidation of NF by $\text{Ti}_3\text{C}_2\text{T}_x$ and H_2O_2 under a hydrothermal condition. **Figure 2a** shows the XRD patterns of the obtained samples. It can be clearly seen that the (104) peak of $\text{Ti}_3\text{C}_2\text{T}_x$ corresponding to the Al layer at 39° disappears and the (002) peak shifts to a small angle by comparison with pristine Ti_3AlC_2 , indicating that $\text{Ti}_3\text{C}_2\text{T}_x$ nanosheets were successfully achieved.^[32] In this work, different contents of $\text{Ti}_3\text{C}_2\text{T}_x$ (2, 5, 8, and 10 mg) were added to explore its effect on the oxidation of NF by H_2O_2 . It is worth noting that no obvious Ni(OH)_2 layer was formed on the surface of NF without the addition of $\text{Ti}_3\text{C}_2\text{T}_x$ (see **Figure S1**, Supporting Information). The as-obtained four integrated electrodes show almost the same XRD patterns. When adding fewer amounts of $\text{Ti}_3\text{C}_2\text{T}_x$ such as 2 and 5 mg, the (002) diffraction peak is not obvious. For samples with 8 and 10 mg of $\text{Ti}_3\text{C}_2\text{T}_x$ added, an obvious (002) peak at 6.25° can be seen, which is a characteristic peak of $\text{Ti}_3\text{C}_2\text{T}_x$. Beyond that, the remaining diffraction peaks in the four electrodes centered at 11.6° , 33.7° , 35.2° , and 59.6° corresponding to the lattice planes of (001), (110), (111), and

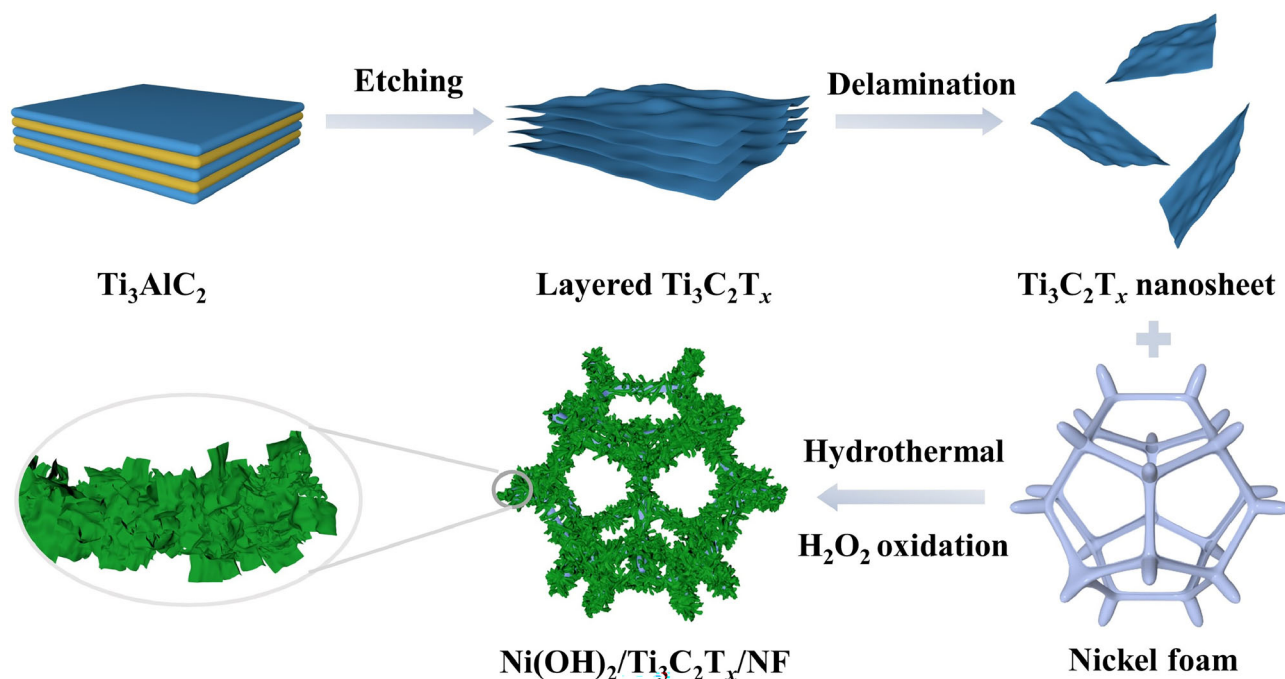


Figure 1. Schematic diagram of the synthesis of $\text{Ni(OH)}_2/\text{Ti}_3\text{C}_2\text{T}_x/\text{NF}$ composite.

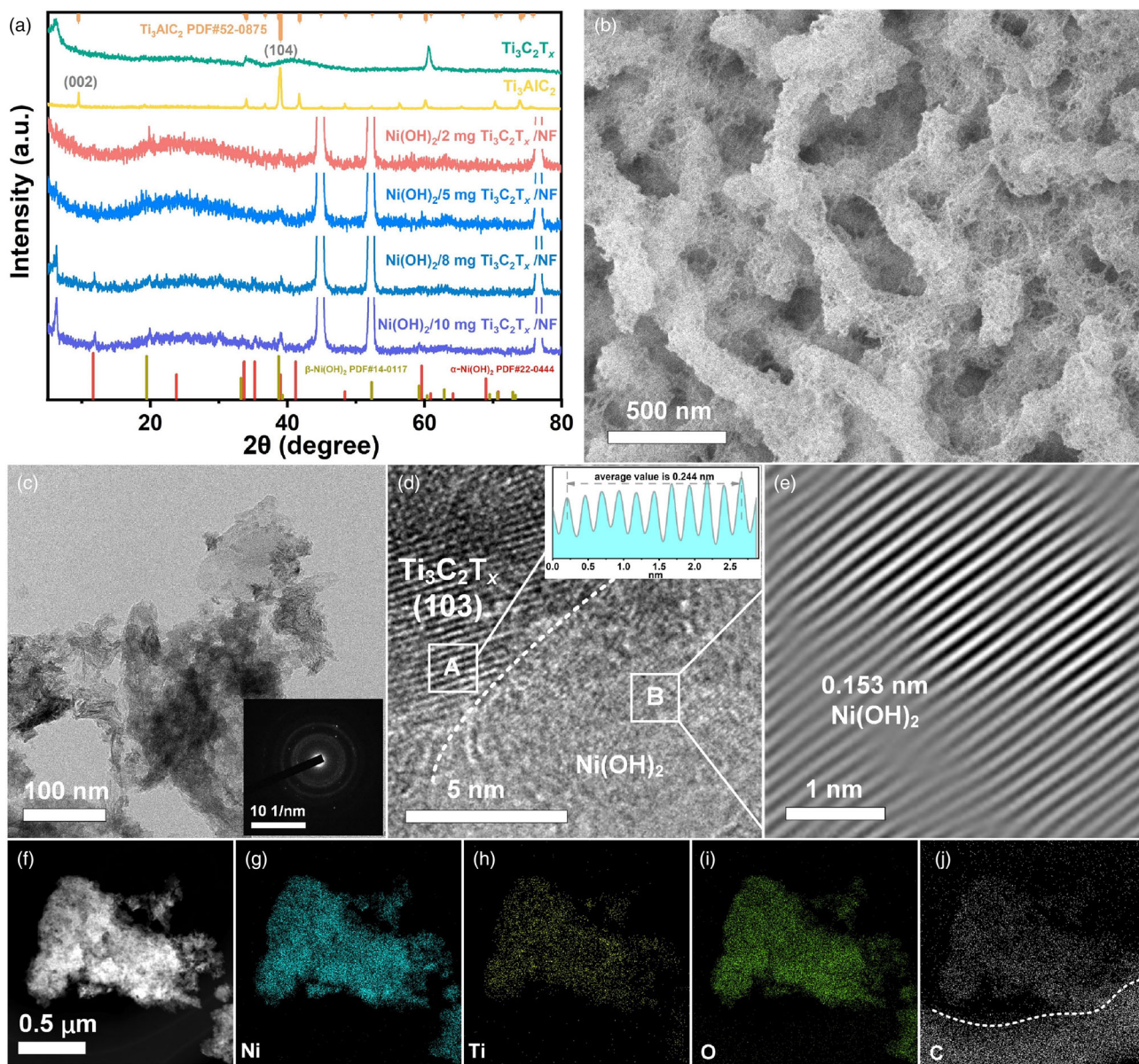


Figure 2. a) XRD patterns of the as-prepared integrated electrodes. Characterization of the 2 mg $\text{Ni(OH)}_2/\text{Ti}_3\text{C}_2\text{T}_x/\text{NF}$: b) SEM image; c) TEM image. Inset: SAED image; d) HRTEM image. Inset: Interplanar spacings of the lattice fringe; e) inverse fast Fourier transform (IFFT) image; f) HAADF image; and g–j) mapping images.

(300) in $3\text{Ni(OH)}_2 \cdot 2\text{H}_2\text{O}$ ($\alpha\text{-Ni(OH)}_2$ phase, JCPDS No. 22-0444); the 19.3° and 38.5° belong to the (001) and (101) crystal planes of $\beta\text{-Ni(OH)}_2$ (JCPDS No. 14-0117), respectively. These results indicate that $\text{Ti}_3\text{C}_2\text{T}_x$ plays an important role in the formation of Ni(OH)_2 , while the amount of it has little effect on the phase composition of the final products, and $\text{Ti}_3\text{C}_2\text{T}_x$ is not oxidized by H_2O_2 in the synthesis process. The latter is different from the usual perception that MXene is easily oxidized in the presence of an oxidant, suggesting that the structure of MXene is relatively stable when it coexists with other components (such as NF) that are more easily oxidized.

The electrode with 2 mg $\text{Ni(OH)}_2/\text{Ti}_3\text{C}_2\text{T}_x/\text{NF}$ was chosen as an example for the following characterizations. As shown in Figure 2b, the SEM image reveals that stacked nanosheet-like cicada-pupa

nanostructures cover all of the NF substrate. To achieve more details of the integrated electrode, the sample was ultrasonically treated in ethanol and peeled off for TEM characterization. From the TEM image in Figure 2c, irregular thick nanosheets were presented. The corresponding SAED pattern (Figure 2c inset) shows that the product is a coexistence phase of single crystal and weak crystallinity. HRTEM image of the sample was further recorded. The lattice fringe spacing of the nanosheet in A site is 0.244 nm (Figure 2d inset) corresponding to the $\text{Ti}_3\text{C}_2\text{T}_x$ (103) plane, respectively. B site in large nanosheet displays weak crystallinity. From the corresponding inverse fast Fourier transform (IFFT) image (Figure 2e), the lattice fringe with a spacing 0.153 nm can be seen, which should be ascribed to $\alpha\text{-Ni(OH)}_2$ (300) face or $\beta\text{-Ni(OH)}_2$ (003) face. Furthermore, HAADF-STEM (Figure 2f)

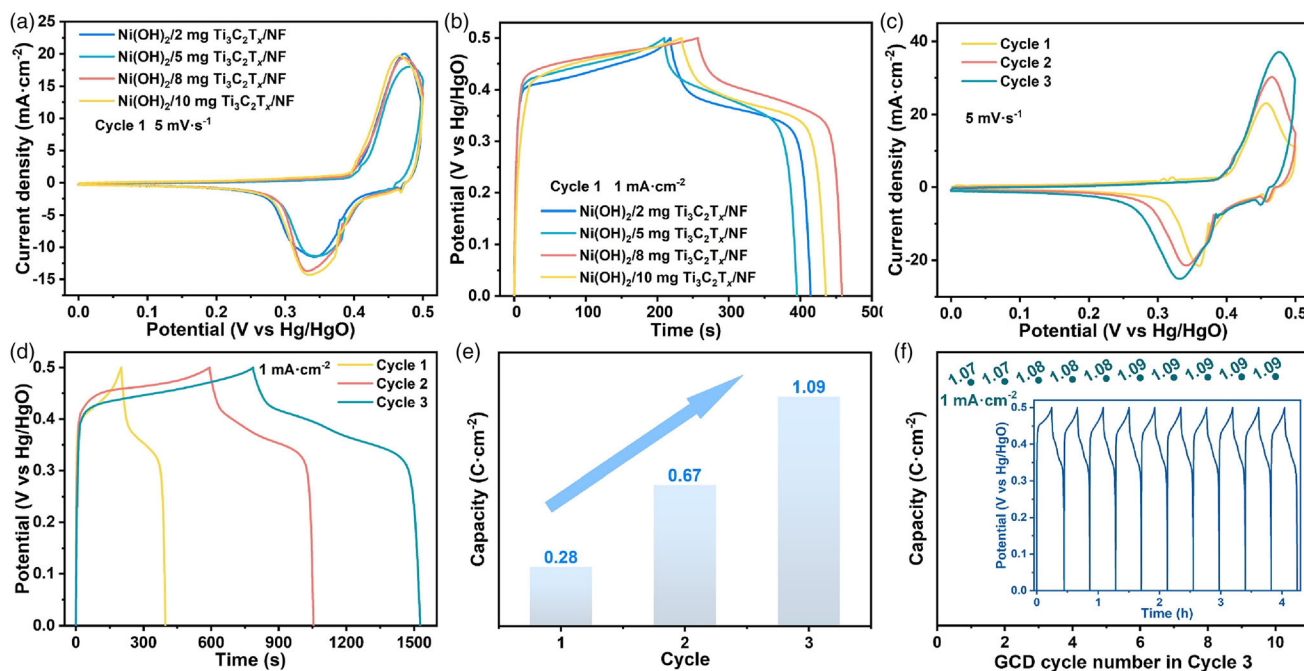


Figure 3. a) Cyclic voltammetry (CV) curves and b) galvanostatic charge/discharge (GCD) curves of the four integrated electrodes after the first electrochemical activation cycle. c) CV curves and d) GCD curves of 2 mg $\text{Ni}(\text{OH})_2/\text{Ti}_3\text{C}_2\text{T}_x/\text{NF}$ at different activation cycles; e) Specific capacity value of 2 mg $\text{Ni}(\text{OH})_2/\text{Ti}_3\text{C}_2\text{T}_x/\text{NF}$ at different activation cycles; f) The last 10-cycle GCD curves of the third cycle and their corresponding capacity value of 2 mg $\text{Ni}(\text{OH})_2/\text{Ti}_3\text{C}_2\text{T}_x/\text{NF}$.

and elemental analysis (Figure 2g–j) demonstrated that Ni, Ti, O, and C elements coexisted and were uniformly distributed throughout the nanosheets. All the above results indicate that $\text{Ni}(\text{OH})_2/\text{Ti}_3\text{C}_2\text{T}_x/\text{NF}$ was successfully prepared by the oxidation of NF with H_2O_2 in the presence of $\text{Ti}_3\text{C}_2\text{T}_x$.

To improve the electrochemical performance of the $\text{Ni}(\text{OH})_2/\text{Ti}_3\text{C}_2\text{T}_x/\text{NF}$, an initial 40 cycles of CV and GCD process were conducted in 1.0 M KOH solution, which is called the first cycle of the electrochemical activation. Figure 3a is the CV curves of four integrated electrodes at a scan rate of 5 mV s^{-1} after the first cycle. It can be seen that the four integrated electrodes show almost identical CV areas and redox peaks, indicating that they have the same electrochemical performance. Similarly, their GCD curves (Figure 3b) exhibit an identical charge–discharge plateau and discharge time at the current density of 1 mA cm^{-2} . The above results show that the addition amount of $\text{Ti}_3\text{C}_2\text{T}_x$ has almost negligible impact on the electrochemical properties of the products, which means the effect of $\text{Ti}_3\text{C}_2\text{T}_x$ on NF-oxidation of H_2O_2 is independent of the addition amount, agreeing well with the XRD results. More interestingly, the electrochemical performance of the integrated electrode dramatically improves with increasing the activation cycle, and the performance reaches a stable state after the third cycle. Taking 2 mg $\text{Ni}(\text{OH})_2/\text{Ti}_3\text{C}_2\text{T}_x/\text{NF}$ as an example, Figure 3c,d shows the CV and GCD curves at different activation cycles, respectively, from which an obvious enhanced electrochemical performance with increasing cycling number can be seen. According to the capacity calculation formula $C = 2I \int V dt / \Delta V$ (I is the current density, t is the discharge time, and ΔV is the voltage window) and galvanostatic discharge curves, the specific capacity value of 2 mg $\text{Ni}(\text{OH})_2/\text{Ti}_3\text{C}_2\text{T}_x/\text{NF}$ increased from 0.28 C cm^{-2} in the first cycle to 0.67 C cm^{-2} in the second cycle, and then to 1.09 C cm^{-2} in the third cycle

(Figure 3e). The same trend was also observed for the other three integrated electrodes with different amounts of $\text{Ti}_3\text{C}_2\text{T}_x$ (Figure S2, Supporting Information). The above results show that the electrochemical performance of $\text{Ni}(\text{OH})_2/\text{Ti}_3\text{C}_2\text{T}_x/\text{NF}$ was successfully enhanced by the electrochemical activation process. Moreover, the electrochemical performance was stabilized after the third cycle, as demonstrated in Figure 3f. Almost the same specific capacity value at 1 mA cm^{-2} can be obtained in the last 10-cycle GCD curves of the third cycle, indicating that the electrochemical activation is over and the performance reaches the optimum.

To explore the reason and mechanism behind the increased capacity performance of 2 mg $\text{Ni}(\text{OH})_2/\text{Ti}_3\text{C}_2\text{T}_x/\text{NF}$ by electrochemical activation, a series of characterizations were carried out. As displayed in Figure S3, Supporting Information, the XRD pattern of electrochemically activated 2 mg $\text{Ni}(\text{OH})_2/\text{Ti}_3\text{C}_2\text{T}_x/\text{NF}$ is similar to the original electrode, indicating that there is no change in phase after the electrochemical activation process. Figure 4a presents the TEM image of electrochemically activated 2 mg $\text{Ni}(\text{OH})_2/\text{Ti}_3\text{C}_2\text{T}_x/\text{NF}$, from which the well-defined ultrathin and nearly transparent nanosheet with a lateral size of several 100 nm can be seen. Moreover, the corresponding HRTEM images of area 1 and area 2 show that the activated sample has a highly crystalline nature, with clearly identified lattice fringe spaces of 0.218 and 0.244 nm corresponding to both the (103) plane of the $3\text{Ni}(\text{OH})_2 \cdot 2\text{H}_2\text{O}$ ($\alpha\text{-Ni}(\text{OH})_2$) phase and $\text{Ti}_3\text{C}_2\text{T}_x$, respectively. As observed by the TEM and HRTEM, it is believed that during the electrochemical activation process, the original irregular weak crystallinity $\text{Ni}(\text{OH})_2$ thick nanosheets can be restructured and form ultrathin nanosheets with good crystallinity, which are beneficial for providing larger surface area and higher electrical conductivity, thereby resulting in the dramatically increased specific capacity. XPS was conducted to

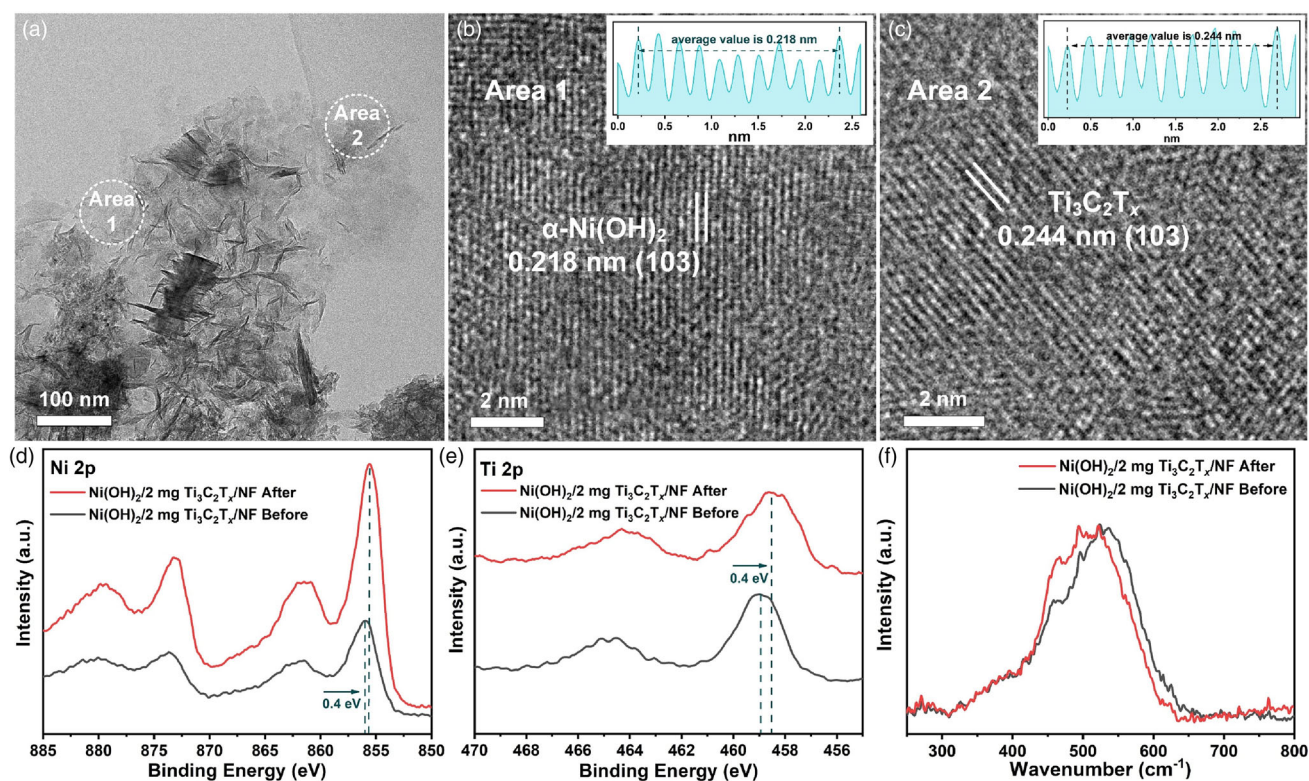


Figure 4. a) TEM image, and b, c) corresponding HRTEM images in Area 1 and Area 2 of electrochemically activated 2 mg Ni(OH)₂/Ti₃C₂T_x/NF. Inset: Interplanar spacings of the lattice fringes. XPS spectra of d) Ni 2p and e) Ti 2p, f) Raman spectra of 2 mg Ni(OH)₂/Ti₃C₂T_x/NF before and after activation.

study the composition and valence states of the 2 mg Ni(OH)₂/Ti₃C₂T_x/NF before and after electrochemical activation. As shown in Figure S4, Supporting Information, Ni, Ti, O, and C elements are detected in the XPS survey of the two samples. Moreover, the elemental contents from XPS reveal the atomic ratio of Ni:Ti is 8.27:1 in the pristine one. Ni 2p spectrum of the pristine sample in Figure 4d shows two peaks located at 856.0 and 873.7 eV accompanied by two satellite peaks, which belong to the characteristic spin-orbit 2p_{3/2} and 2p_{1/2}, showing that the valence state of Ni is +2. However, after the electrochemical activation, an obvious 0.4 eV shift of Ni 2p toward lower binding energy is observed in the electrochemically activated sample. Moreover, the same shift phenomenon occurs in the Ti 2p of both samples. Such apparent binding energy shift of both Ni and Ti atoms indicates that the electronic structure of the components is changed by the electrochemical activation, which is conducive to improving the reaction activity. Specifically, since the charge storage of the integrated electrode mainly relies on the redox reaction between Ni(OH)₂/NiOOH couple, the lower oxidation state of Ni can realize more electron transfer and thus store more capacity.^[5] Raman spectroscopy was employed to further confirm the structural change in the sample before and after electrochemical activation, as shown in Figure 4f. Compared with the pristine one, no impurity peak is found in the Raman spectrum of the activated sample, which indicates that there is no new phase formed during the electrochemical activation, agreeing well with the XRD results. However, the peaks located at 400–600 cm⁻¹ indexed to the stretching vibrations of the Ni–O bond in Ni(OH)₂ crystal structure show a shift toward a lower wavenumber than that of pristine one, which further verifies the structure change after electrochemical

activation. All the above results reveal that the structure including crystallinity, morphology, and electronic state of the integrated electrode is transformed after electrochemical activation.

To fully assess the performance improvement effect after three-cycle electrochemical activation, the electrochemical performances of the other three activated (5, 8, and 10 mg) Ni(OH)₂/Ti₃C₂T_x/NF were also systematically analyzed in three-electrode configuration. For comparison, the electrochemical performances of commercial NF and sample obtained without the addition of Ti₃C₂T_x (named Ni(OH)₂/0 mg Ti₃C₂T_x/NF) were also tested. Figure 5a shows the CV curves of these samples, from which the four activated samples exhibit almost the same CV curve area and redox peak intensity, indicating a similar capacity performance and redox reaction kinetics process, which is further confirmed by the GCD curves. As shown in Figure 5b, they have almost same potential-time curves and discharge times, and the capacity values are in the range of 1.07–1.09 C cm⁻². Besides, very similar electrochemical kinetic behaviors of the four activated samples were revealed by the Nyquist plot and Bode phase angle plot, as displayed in Figure 5c. Notably, as observed from CV, GCD and EIS curves, the commercial NF and Ni(OH)₂/0 mg Ti₃C₂T_x/NF show the same and negligible capacity performances, further indicating that Ti₃C₂T_x has a positive effect on the formation of Ni(OH)₂. Considering that the addition amount of Ti₃C₂T_x in the range of 2–10 mg has negligible influence on the electrochemical properties of the products before and after electrochemical activation, we concluded that: i) Ti₃C₂T_x plays a catalytic role in the oxidation of NF by H₂O₂, and the addition amount of 2 mg is enough; ii) the contribution of capacity mainly comes from the Ni(OH)₂ in situ generated on the NF substance; iii) the regulation

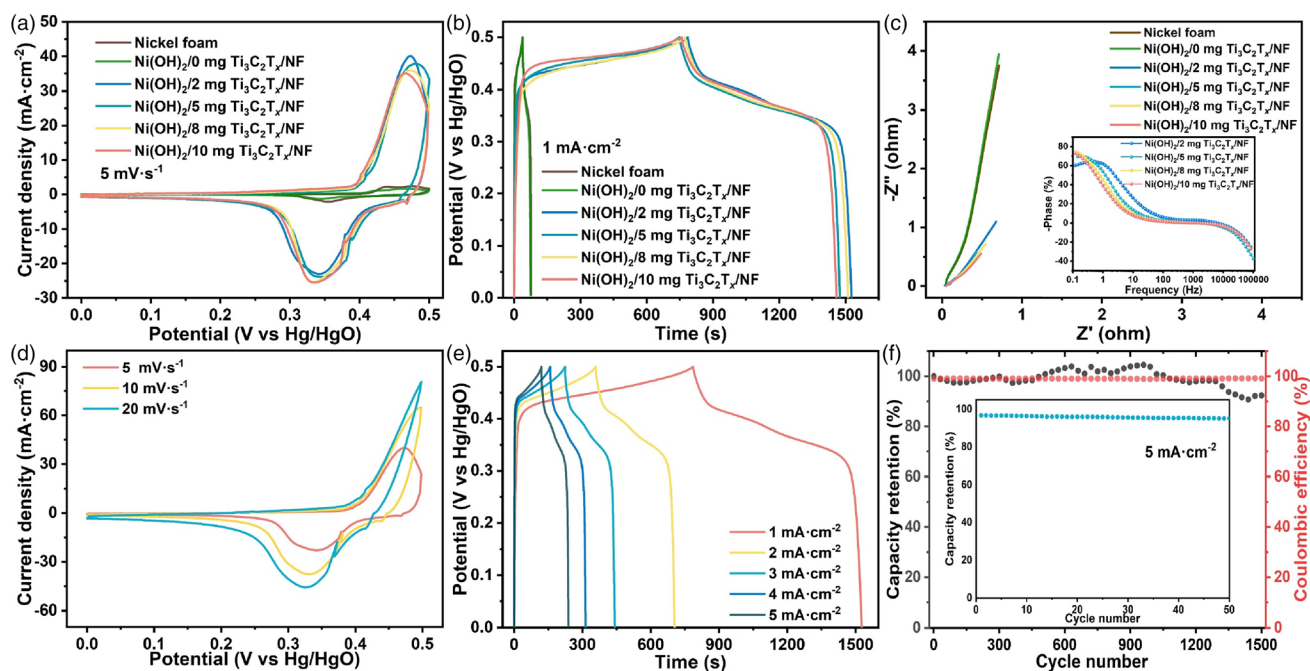


Figure 5. a) Cyclic voltammetry (CV) curves, b) galvanostatic charge/discharge (GCD) curves, and c) EIS plot of the samples after electrochemical activation. Inset: the Bode phase angle plot. d) CV curves at different scan rates, e) GCD curves at different current densities and f) Cycling performance at 5 mA cm^{-2} of activated $2 \text{ mg Ni(OH)}_2/\text{Ti}_3\text{C}_2\text{T}_x/\text{NF}$.

of the morphology, crystallinity, and electronic structure of Ni(OH)_2 is responsible for the enhancement of capacity performance during the electrochemical activation process.

CV curves at different scan rates and GCD curves at different current densities of $2 \text{ mg Ni(OH)}_2/\text{Ti}_3\text{C}_2\text{T}_x/\text{NF}$ were further conducted. As shown in Figure 5d, with the increase in the scan rates, similar CV curve shapes are observed, indicating good electrochemical reversibility. Moreover, the value of the index b is calculated by the formula $i = av^b$ to be 0.5, which points to the battery-type characteristic (Figure S5, Supporting Information).^[33] GCD curves (Figure 5e) at current densities of $1\text{--}5 \text{ mA cm}^{-2}$ show its good symmetry and Coulombic efficiencies. In addition, the corresponding area-specific capacities were calculated to be 1.09, 1.02, 0.96, 0.91, and 0.85 C cm^{-2} , respectively. Compared with 1 mA cm^{-2} , the capacity retention at 5 mA cm^{-2} is 78.0%, which proves the good rate performance. Moreover, the capacity retention of 92.4% and the Coulomb efficiency of 99% were achieved of $2 \text{ mg Ni(OH)}_2/\text{Ti}_3\text{C}_2\text{T}_x/\text{NF}$ after 1500 charge/discharge cycles at a current density of 5 mA cm^{-2} (Figure 5f), showing the excellent cycling stability. Besides, the GCD curves of the first 50 cycles in the inset show that the capacity value basically remains unchanged, further confirming that the activation process has been completed after three cycles.

To evaluate the possibility of the as-prepared $2 \text{ mg Ni(OH)}_2/\text{Ti}_3\text{C}_2\text{T}_x/\text{NF}$ for practical application, a hybrid supercapacitor (HSC) was assembled for electrochemical measurement by using $2 \text{ mg Ni(OH)}_2/\text{Ti}_3\text{C}_2\text{T}_x/\text{NF}$ as the cathode and commercial activated carbon (AC) as the anode. The loading of AC is calculated based on the formula $C_1 \times S_1 = C_2 \times S_2$, (C is the area-specific capacity, and S is the area) to obtain a high-performance assembled device. To determine the operating potential window, the CV curves of $2 \text{ mg Ni(OH)}_2/\text{Ti}_3\text{C}_2\text{T}_x/\text{NF}$ and AC were conducted at a scan rate of 5 mV s^{-1} . As shown in Figure 6a, the commercial AC electrode shows the typical

double-layer capacitance feature with a nearly rectangular shape in the potential window of -1.0 to 0 V , while the $2 \text{ mg Ni(OH)}_2/\text{Ti}_3\text{C}_2\text{T}_x/\text{NF}$ displays battery-type capacitance performance at potentials of $0\text{--}0.5 \text{ V}$. Thus, the theoretical working potential of the HSC device is $0\text{--}1.5 \text{ V}$. As presented in Figure 6b, no obvious polarization phenomenon occurs in the CV curves of the HSC device when the potential increases to 1.5 V . Moreover, the combined capacitive features of both battery-type capacity behavior and electrical double-layer can be seen from the CV curves. Figure 6c shows that the shape of CV curves still maintains when the scan rate increases from 5 to 50 mV s^{-1} , indicating the good rate capability. The GCD curves at different current densities of the HSC device are shown in Figure 6d. According to the discharge curves, the area-specific capacity of the assembled device was determined to be 0.43, 0.39, 0.35, 0.31, and 0.27 C cm^{-2} at current densities of $1\text{--}5 \text{ mA cm}^{-2}$, respectively. Meanwhile, the faradic/energy efficiency of the HSC device is calculated to be 79.3% and 65.2% from the GCD curves recorded at current densities of 1 and 5 mA cm^{-2} , indicating the good rate property and reversibility of this device. Furthermore, the HSC device provides a high energy density of 0.1 mWh cm^{-2} at a power density of 0.97 mW cm^{-2} . For practical application, the leakage current and self-discharge characteristics of this HSC device were also estimated. As displayed in Figure 6e, the HSC device requires a current of 80 A cm^{-2} to maintain a potential of 1.2 V . The self-discharge characteristic of this device maintains the potential of 1.2 and 0.97 V when it was fully charged after 2 and 5 h of self-discharge, respectively, which shows the HSC device is in good health. Besides, the HSC demonstrates excellent cycling stability (Figure 6f) with specific capacitance retention of 110% and Coulombic efficiency of 98.9% after 5000 GCD cycles at 4 mA cm^{-2} . Some additional characterizations including TEM, XRD, and XPS were performed to confirm the maintenance of phase, morphology, and valence state of $2 \text{ mg Ni(OH)}_2/\text{Ti}_3\text{C}_2\text{T}_x/\text{NF}$ after the stability test (Figure S6, Supporting Information), which

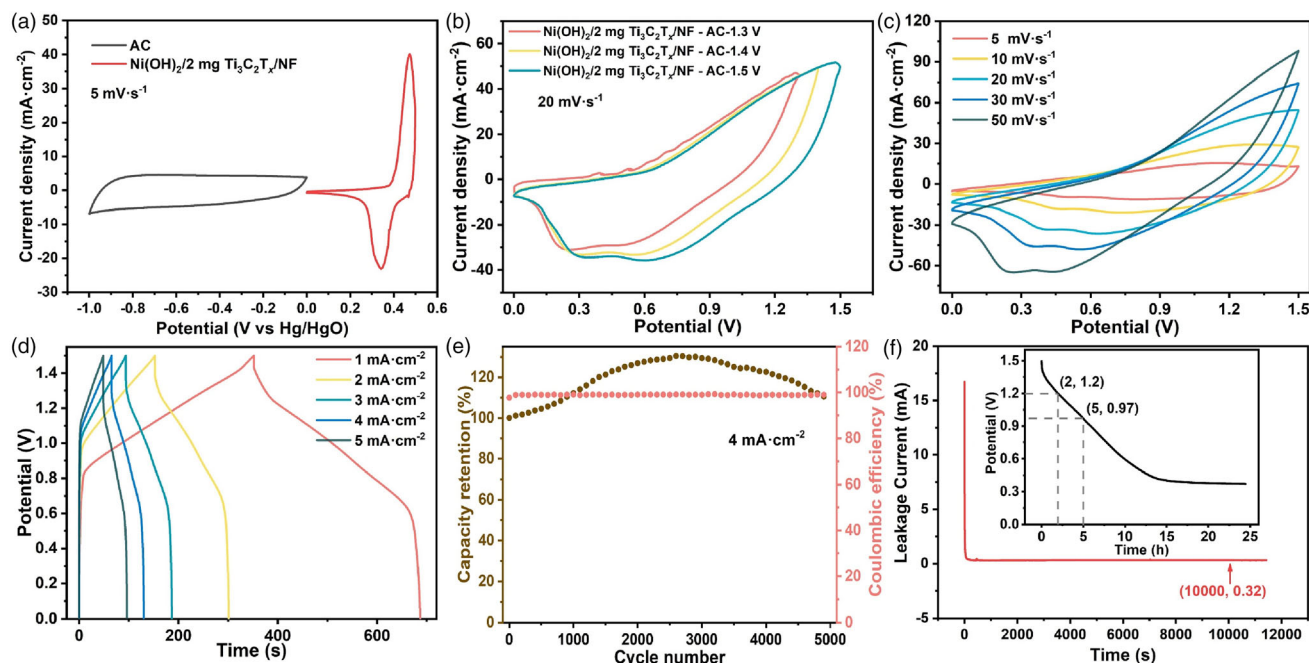


Figure 6. a) Cyclic voltammetry (CV) curves of 2 mg Ni(OH)₂/Ti₃C₂T_x/NF and activated carbon electrode. Performance investigation of 2 mg Ni(OH)₂/Ti₃C₂T_x/NF//AC/NF hybrid supercapacitors. b) CV curves at various potential windows. c) CV curves at different scan rates. d) Galvanostatic charge/discharge (GCD) curves at different current densities. e) Cycling performance at 4 mA cm⁻². f) Leakage current and self-discharge curves.

shows the superior chemical stability. All the above results reveal the excellent electrochemical performance of Ni(OH)₂/Ti₃C₂T_x/NF//AC/NF HSC.

3. Conclusion

In summary, the Ni(OH)₂/Ti₃C₂T_x/NF integrated electrodes were successfully synthesized through a facile hydrothermal method, in which the Ni foam acts as a nickel source directly. The Ti₃C₂T_x is not only used as a conductive substance in the composite electrode, but also as a catalyst to promote the in situ oxidation of nickel foam by H₂O₂. Interestingly, the capacity of the integrated electrode increases by a factor of three after electrochemical activation, which is mainly attributed to the structural transformation including crystallinity, electronic structure, and morphology of Ni(OH)₂ during the activation process. The activated electrode delivers well discharge specific capacity of 1.09 C cm⁻² at 1 mA cm⁻², excellent rate performance, and good cycling stability. Furthermore, the hybrid supercapacitor (HSC) assembled with 2 mg Ni(OH)₂/Ti₃C₂T_x/NF electrode and AC/NF electrode provides an energy density of 0.1 mWh cm⁻² at a power density of 0.97 mW cm⁻², and the capacity retention rate is 110% after 5000 charge–discharge cycles. This work provides a new approach for the large-scale production of battery-type Ni(OH)₂-based electrode materials for hybrid supercapacitors.

4. Experimental Section

Experimental details, characterization, and electrochemical measurements are provided in [Supporting Information](#).

Acknowledgements

CX. and L.D. contributed equally to the work. This work was supported by the NSF of China (Nos. 21971143, 21805165, 22209098) and the 111 Project (D20015), the major research and development project of Hubei Three Gorges Laboratory (2022-3), and the Natural Science Foundation of Hubei Province (2022CFB326).

Supporting Information

Supporting Information is available from the Wiley Online Library or from the author.

Keywords

electrochemical activation, hybrid supercapacitors, Ni(OH)₂, Ti₃C₂T_x

Received: May 18, 2023

Revised: July 11, 2023

Published online: July 12, 2023

- [1] D. P. Chatterjee, A. K. Nandi, *J. Mater. Chem. A* **2021**, *9*, 15880.
- [2] J. Zhou, S. Zhang, Y.-N. Zhou, W. Tang, J. Yang, C. Peng, Z. Guo, *Electrochem. Energy Rev.* **2021**, *4*, 219.
- [3] P. Lu, D. Wu, L. Chen, H. Li, F. Wu, *Electrochem. Energy Rev.* **2022**, *5*, 3.
- [4] X. Luo, S. Chen, T. Hu, Y. Chen, F. Li, *SusMat* **2021**, *1*, 211.
- [5] H. Liu, X. Liu, S. Wang, H.-K. Liu, L. Li, *Energy Storage Mater.* **2020**, *28*, 122.
- [6] Y. Liu, N. Fu, G. Zhang, M. Xu, W. Lu, L. Zhou, H. Huang, *Adv. Funct. Mater.* **2017**, *27*, 1605307.

- [7] H.-C. Chen, L.-Y. Hou, C. He, P.-J. Laing, C.-Y. Huang, W.-S. Kuo, *ACS Appl. Energy Mater.* **2022**, *5*, 8262.
- [8] S. Natarajan, M. Ulaganathan, V. Aravindan, *J. Mater. Chem. A* **2021**, *9*, 15542.
- [9] D. S. Hall, D. J. Lockwood, C. Bock, B. R. MacDougall, *Proc. Royal Soc. A Math. Phys. Eng. Sci.* **2015**, *471*, 20140792.
- [10] H. Chai, X. Peng, T. Liu, X. Su, D. Jia, W. Zhou, *RSC Adv.* **2017**, *7*, 36617.
- [11] L. Wang, X. Li, T. Guo, X. Yan, B. K. Tay, *Int. J. Hydrogen Energy* **2014**, *39*, 7876.
- [12] Z. Qin, J. Liu, B. Sun, H. Zou, L. Chen, Y. Xu, Y. Cao, C. Chen, *Electrochim. Acta* **2022**, *435*, 141370.
- [13] S. Xu, X. Li, Z. Yang, T. Wang, W. Jiang, C. Yang, S. Wang, N. Hu, H. Wei, Y. Zhang, *ACS Appl. Mater. Interfaces* **2016**, *8*, 27868.
- [14] B. Dong, M. Li, S. Chen, W. Ding, W. Wei, G. Gao, S. Ding, *ACS Appl. Mater. Interfaces* **2017**, *9*, 17890.
- [15] Z. Pan, F. Cao, X. Hu, X. Ji, *J. Mater. Chem. A* **2019**, *7*, 8984.
- [16] L. Xu, L. Zhang, B. Cheng, J. Yu, *Carbon* **2019**, *152*, 652.
- [17] J. Lu, H. Duan, Y. Zhang, G. Zhang, Z. Chen, Y. Song, R. Zhu, H. Pang, *ACS Appl. Mater. Interfaces* **2022**, *14*, 25878.
- [18] X. Liu, Y. Yang, X. Xing, T. Zou, Z. Wang, Y. Wang, *ChemElectroChem* **2018**, *5*, 434.
- [19] X. Xiong, D. Ding, D. Chen, G. Waller, Y. Bu, Z. Wang, M. Liu, *Nano Energy* **2015**, *11*, 154.
- [20] L. Lyu, J. Hu, K. Cheng, D. Lin, K. Li, Z. Lu, H. Yao, L. Zhou, *Carbon* **2022**, *188*, 177.
- [21] C. Deng, J. He, G. Wang, K. Wang, W. Dong, X. Hong, *Appl. Surf. Sci.* **2023**, *616*, 156526.
- [22] G. Liu, Y. Qin, Y. Lyu, M. Chen, P. Qi, Y. Lu, Z. Sheng, Y. Tang, *Chem. Eng. J.* **2021**, *426*, 131248.
- [23] D. Ye, Y. Yu, J. Tang, L. Liu, Y. Wu, *Nanoscale* **2016**, *8*, 10406.
- [24] Y. Li, J. Zhou, J. Song, X. Liang, Z. Zhang, D. Men, D. Wang, X.-E. Zhang, *Biosens. Bioelectron.* **2019**, *144*, 111534.
- [25] Y. Zhang, Y. Liu, Z. Sun, J. Fu, S. Cheng, P. Cui, J. Zhou, Z. Zhang, X. Pan, W. Han, E. Xie, *J. Mater. Chem. A* **2019**, *7*, 21290.
- [26] X. Zou, J. Hao, Y. Zhou, F. Chen, Q. Hu, B. Xiang, H. Yang, M. Deng, *J. Alloys Compd.* **2021**, *855*, 157332.
- [27] X. Yang, Y. Tian, S. Li, Y.-P. Wu, Q. Zhang, D.-S. Li, S. Zhang, *J. Mater. Chem. A* **2022**, *10*, 12225.
- [28] M. S. Javed, X. Zhang, S. Ali, A. Mateen, M. Idrees, M. Sajjad, S. Batool, A. Ahmad, M. Imran, T. Najam, W. Han, *Nano Energy* **2022**, *101*, 107624.
- [29] M. Hu, H. Zhang, T. Hu, B. Fan, X. Wang, Z. Li, *Chem. Soc. Rev.* **2020**, *49*, 6666.
- [30] X. Yang, C. Xu, S. Li, Y.-P. Wu, X.-Q. Wu, Y.-M. Yin, D.-S. Li, *J. Colloid Interface Sci.* **2022**, *617*, 633.
- [31] Q. Jiang, N. Kurra, M. Alhabeib, Y. Gogotsi, H. N. Alshareef, *Adv. Energy Mater.* **2018**, *8*, 1703043.
- [32] M. Naquib, M. Kurtoglu, V. Presser, J. Lu, J. Niu, M. Hen, L. Hultman, Y. Gogotsi, M. W. Barsoum, *Adv. Mater.* **2011**, *23*, 4248.
- [33] Y. Wang, Y. Song, Y. Xia, *Chem. Soc. Rev.* **2016**, *45*, 5925.